

in the films grown on the rolled-textured Ni. These pinning sites may be associated with growth-induced defect structures (25) or low-angle grain boundary pinning, or both (16, 17). The $J_c(77\text{ K}, H)$ behavior for $\text{Bi}_2\text{Sr}_2\text{Ca}_2\text{Cu}_3\text{O}_y$ (Bi-2223)/Ag (26) and $\text{TlBa}_2\text{Ca}_2\text{Cu}_3\text{O}_{8+x}$ (Tl-1223)/YSZ (27) tapes are also shown for comparison.

The temperature (T) dependence of J_c , measured in magnetic fields of 0, 3, and 8 T applied parallel to the YBCO c axis, is shown in Fig. 4. The $J_c(T)$ behavior for the YBCO films on the rolled-textured Ni tapes is comparable with that observed for epitaxial films on oxide single crystals, which is consistent with the absence of high-angle grain boundaries in the YBCO film. For comparison, we also show data for conventional low- T_c superconducting NbTi and Nb_3Sn wires (T_c is the superconducting transition temperature) (28) as well for $\text{Bi}_3\text{Sr}_2\text{CaCu}_2\text{O}_x$ (Bi-2212)/Ag (29), Bi-2223/Ag (30), and Tl-1223/poly-YSZ (27) HTS wires and tapes. Clearly, the performance of the epitaxial YBCO on rolled-textured Ni tape, in terms of J_c , is far superior to that of these other superconducting wire technologies, both for zero-magnetic field and high-magnetic field applications. In particular, the zero-field J_c of the YBCO on rolled Ni at 77 K is significantly higher than the J_c of state-of-the-art Bi-2223, Bi-2212, or Tl-1223 wires and tapes at 4.2 K. In addition, $J_c(T, H = 8\text{ T})$ for the YBCO/RABiTS is higher than $J_c(T, H = 0)$ for the Bi-2223/Ag and Tl-1223/YSZ wires in zero field at all $T < 65\text{ K}$. At $T < 40\text{ K}$, $J_c(H)$ for these films is greater than for conventional low- T_c superconductors, such as NbTi and Nb_3Sn , operating at 4.2 K. Thus, the use of rolling textured metal substrates, coupled with the epitaxial growth of appropriate buffer layer architectures and superconducting films, represents a viable means for producing long superconducting tapes for high-current, high-field applications at 77 K, particularly if high values of the "engineering" J_c , defined as the critical current per total conductor cross-sectional area (including substrate thickness), can be realized with thinner substrates or thicker YBCO films.

REFERENCES AND NOTES

1. J. W. Ekin, K. Salama, V. Selvamanickam, *Nature* **350**, 26 (1991).
2. D. T. Shaw, *Mater. Res. Soc. Bull.* **17**, 39 (1992); E. E. Hellstrom, *ibid.*, p. 45.
3. J. M. Phillips, *J. Appl. Phys.* **79**, 1829 (1996).
4. D. Dimos, P. Chaudhari, J. Mannhart, F. K. LeGroves, *Phys. Rev. Lett.* **61**, 1653 (1988).
5. D. Dimos, P. Chaudhari, J. Mannhart, *Phys. Rev. B* **41**, 4038 (1990).
6. D. P. Norton *et al.*, *Appl. Phys. Lett.* **57**, 1164 (1990).
7. Z. G. Ivanov *et al.*, *ibid.* **59**, 3030 (1991).
8. R. Gross and B. Mayer, *Physica C* **180**, 235 (1991).

9. M. F. Chisholm and S. J. Pennycook, *Nature* **351**, 47 (1991).
10. M. Kawasaki *et al.*, *Appl. Phys. Lett.* **62**, 417 (1993).
11. E. Sarnelli, P. Chaudhari, W. Y. Lee, E. Esposito, *ibid.* **65**, 362 (1994).
12. S. E. Babcock, X. Y. Cai, D. C. Larbalestier, D. L. Kaiser, *Nature* **347**, 167 (1990).
13. D. K. Christen *et al.*, in *Superconductivity and Its Applications*, H. S. Kwok, D. T. Shaw, M. J. Naughton, Eds. (American Institute of Physics, New York, 1993), vol. 273, p. 24.
14. M. Rupp, A. Gupta, C. C. Tsuei, *Appl. Phys. Lett.* **67**, 291 (1995).
15. Y. Iijima, N. Tanabe, O. Kohno, Y. Ikono, *ibid.* **60**, 769 (1992).
16. R. P. Reade, P. Berdahl, R. E. Russo, S. M. Garrison, *ibid.* **61**, 2231 (1992).
17. X. D. Wu *et al.*, *ibid.* **67**, 2397 (1995).
18. M. Fukutomi, S. Aoki, K. Komori, R. Chatterjee, H. Maeda, *Physica C* **219**, 333 (1994).
19. F. Yang, E. Narumi, S. Patel, D. T. Shaw, *ibid.* **244**, 299 (1995).
20. H. Makita, S. Hanada, O. Izumi, *Acta Metall.* **36**, 403 (1988).
21. A. Goyal *et al.*, *Appl. Phys. Lett.* **69**, 1795 (1996).
22. N. N. Khoi, W. W. Smeltzer, J. D. Embury, *J. Electrochem. Soc.* **122**, 1495 (1975).
23. E. D. Specht *et al.*, *Physica C* **226**, 76 (1994).
24. J. D. Budai, R. T. Young, B. S. Chao, *Appl. Phys. Lett.* **62**, 1836 (1993).
25. D. H. Lowndes *et al.*, *Phys. Rev. Lett.* **74**, 2355 (1995).
26. S. Kobayashi, T. Kaneko, T. Kato, J. Fujikami, K. Sato, *Physica C* **258**, 336 (1996).
27. J. E. Tkaczyk *et al.*, *Appl. Phys. Lett.* **62**, 3031 (1993).
28. D. R. Tilley and J. Tilley, *Superfluidity and Superconductivity* (IOP Publishing, Bristol, UK, ed. 3, 1990), p. 235.
29. R. Wesche, *Physica C* **246**, 186 (1995).
30. P. Haldar, J. G. Hoehn Jr., J. A. Rice, M. S. Walker, L. R. Motowidlo, *Appl. Phys. Lett.* **61**, 604 (1992).
31. This research was sponsored by ORNL, managed by Lockheed Martin Energy Research Corporation, for the U.S. Department of Energy Office of Energy Efficiency and Renewable Energy and Office of Energy Research, under contract DE-AC05-96OR22464.

1 July 1996; accepted 30 August 1996

Creation of Nanocrystals Through a Solid-Solid Phase Transition Induced by an STM Tip

Jian Zhang,* Jie Liu,* Jin Lin Huang, Philip Kim, Charles M. Lieber†

A scanning tunneling microscope (STM) was used to fabricate T-phase tantalum diselenide (TaSe_2) nanocrystals with sizes ranging from 7 to more than 100 nanometers within the surface layer of 2H- TaSe_2 crystals at liquid helium temperature. Atomic-resolution images elucidate the structural changes between T- and H-phase regions and were used to develop an atomic model that describes a pathway for the production of T-phase nanocrystals from the H-phase crystal precursor through a solid-solid phase transition. The size-dependent properties of these nanocrystals may lead to improved understanding of the physics of charge density waves in small structures.

The development of new methods for the preparation of nanostructures is important in both meso- and nanoscale research because it is often the creation of these structures that limits studies of potentially interesting physical phenomena. Scanned probe microscopes, such as STMs and atomic force microscopes (AFMs), can in principle both create and probe the properties of very small nanoscale structures. For example, the STM has been used to manipulate individual atoms and molecules into structures (1–4), to probe quantum behavior in several nanostructures (5, 6), and to lithographically pattern surfaces (7, 8). The AFM has also been used to create nanostructures, including electronic (9) and mechanical (10) devices, by selective oxidation and nanomachining.

J. Zhang, J. Liu, J. L. Huang, Department of Chemistry, Harvard University, Cambridge, MA 02138, USA.
P. Kim and C. M. Lieber, Department of Chemistry and Division of Applied Sciences, Harvard University, Cambridge, MA 02138, USA.

*These authors contributed equally to this work.

†To whom correspondence should be addressed.

We report here an approach for the fabrication of nanostructures that uses the tip of an STM to drive a solid-solid phase transition in which 2H- TaSe_2 is transformed locally to nanometer-scale domains of T-phase TaSe_2 . Both 1T- and 2H- TaSe_2 are layered materials consisting of covalently bonded two-dimensional (2D) Se–Ta–Se layers in which the Se atom sheets exhibit a hexagonal close-packed structure and the Ta atoms are in octahedral (1T) or trigonal prismatic (2H) holes defined by the two Se sheets. The 3D structure of these materials consists of stacks of the three-atom layers, . . . Se–Ta–Se/Se–Ta–Se . . . , that are held together by weak dispersion forces (11, 12). The structural parameters of 2H- TaSe_2 ($a = 3.43\text{ \AA}$; $c/2 = 6.35\text{ \AA}$) and 1T- TaSe_2 ($a = 3.48\text{ \AA}$; $c = 6.26\text{ \AA}$) are similar. The electronic properties of these two phases, which are defined primarily by trigonal prismatic or octahedral bonding in a single layer, are quite distinct: 2H- TaSe_2 exhibits a weak charge density wave (CDW) that forms at 122 K and becomes

commensurate with the atomic lattice ($3a$ by $3a$) at 90 K, whereas 1T-TaSe₂ exhibits a very strong CDW that forms at >600 K and becomes commensurate ($\sqrt{13}a$ by $\sqrt{13}a$, R 13.9°, where R is the degree of rotation of the CDW relative to the atomic lattice) at 473 K. We found that we could produce at 4.8 K nanocrystals of T-phase TaSe₂ in single crystals of 2H-TaSe₂ by increasing the local electric field above a threshold value. Atomic-resolution images of the nanocrystals and surrounding region demonstrate that the nanocrystals are T-phase material. These images elucidate the atomic changes at the boundary between the T-phase nanocrystal and the H-phase TaSe₂ and have been used to develop an atomic model of this structural transformation. In addition, investigations of the dependence of nanocrystal formation on applied voltage and on the degree of separation between the sample and tip show that the size of the resulting nanocrystals can be controlled by the magnitude of the applied electric field.

Experiments were carried out with an ultrahigh-vacuum (UHV) STM at 4.8 K. The bias voltage in all of these experiments was applied to the tip. High-quality 2H-TaSe₂ single crystals were grown by iodine vapor transport and characterized by x-ray diffraction, magnetic susceptibility, and resistivity measurements (11). Single crystals of 2H-TaSe₂ were cleaved in UHV within the room-temperature region of our STM system and were then transferred in UHV to the 4.8 K stage of the STM.

Two single crystals were used in our studies, and we examined ~ 10 distinct surfaces on these crystals in separate experiments by cleaving as described above.

The results from these experiments were all similar. A typical large-scale image of the cleaved 2H-TaSe₂ crystal at 4.8 K (Fig. 1A) shows both the hexagonal atomic lattice of the surface Se atom sheet and the expected $3a$ by $3a$ superlattice corresponding to the commensurate CDW state in 2H-TaSe₂ (11, 12). After recording this image, we positioned the STM tip at the center of the image and momentarily increased the electric field between the tip and sample by raising the bias voltage to -1.30 V and decreasing the tip-sample separation (13). The image of the crystal surface after this modification step (Fig. 1B) shows significant changes. In particular, we observed a roughly hexagonal region, 35 nm in diameter, at the center of the image that exhibits a large corrugation amplitude with a lattice constant of 1.25 nm. This spacing was similar to but larger than the 1.03 nm wavelength (λ) of the CDW in 2H-TaSe₂. The orientations of each of the distinct regions of the high-amplitude lattice were also rotated $\sim \pm 14^\circ$ relative to the weak $3a$ by $3a$ CDW superlattice of the surrounding 2H-TaSe₂ crystal. The STM modification procedure and resulting structural changes (Fig. 1B) were quite reproducible; that is, the success probability can approach 90% (14).

A reasonable explanation for these observations is that the central hexagonal region corresponds to a nanocrystal of T-phase TaSe₂ (it is well known that 1T-TaSe₂ exhibits a large-amplitude CDW that is rotated 13.9° relative to the atomic lattice) (11, 12). We have confirmed this proposal using atomic-resolution images (Fig. 2A). The atomic lattices in both the modified and surrounding regions exhibit hexagonal meshes with the same lattice

constant ($a \sim 3.4$ Å) and orientation. The atomic lattices in both regions do, however, have a relative shift across the interface separating the two regions. These results are consistent with the known lattice constants of the T- and H-phases and the fact that the H-phase can be converted to the T-phase through a coherent shift of one of the Se atom sheets in a Se-Ta-Se layer. Examination of the nanocrystal CDW superlattice and atomic lattice also confirms that the CDW forms the $\sqrt{13}a$ by $\sqrt{13}a$, R 13.9° superlattice expected for the commensurate state of single-crystal 1T-TaSe₂ (11, 12). In addition, cross-sectional profiles (for example, Fig. 2B) taken through the T-phase nanocrystal and surrounding H-phase region demonstrate that both phases are in the same layer; that is, there is no step observed at the boundary between the two regions. Taken together, these results suggest that the central T-phase TaSe₂ nanocrystal was created by a

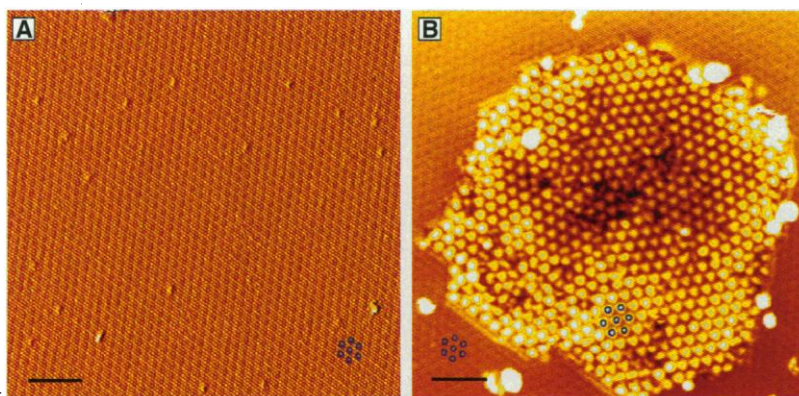


Fig. 1. (A) STM image of a single crystal of 2H-TaSe₂. The atomic lattice and $3a$ by $3a$ CDW superlattice are visible. (B) Image of the surface region in (A) after a voltage modification pulse of -1300 mV had been applied to the tip (13). The probability of crystal modification was similar with the use of either negative or positive applied voltages. Both images were recorded with tunneling currents of 50 pA and bias voltages applied to the tip of 500 mV. The small open blue circles in (A) and (B) highlight the orientations of the $3a$ by $3a$ CDW superlattices and the orientation of one domain of the new superlattice created after the modification step. Scale bars, 5 nm.

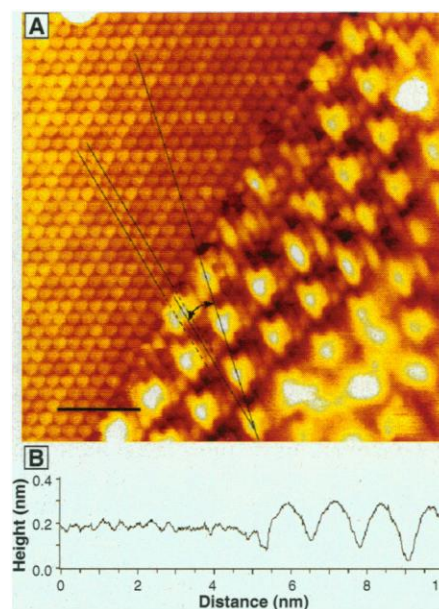


Fig. 2. (A) Atomically resolved topographic image of the interface between H-phase and T-phase regions in TaSe₂. The upper left region is H-phase TaSe₂; the lower right region is the T-phase region. The large-amplitude $\sqrt{13}a$ by $\sqrt{13}a$ CDW in this latter region obscures some of the atomic structure. The longer black line running across the image from upper left to lower right corresponds to the cross section in (B). This line follows the direction of the T-phase CDW superlattice and is rotated 13.9° relative to the atomic lattice in the H-phase region. The short black lines in the lower right half of the image mark the direction of the atomic lattice rows approaching the H-T interface from both H-phase and T-phase regions. The lines corresponding to the lattice rows in the two regions are parallel but are displaced by a fraction of a lattice constant relative to each other. Scale bar, 2 nm. (B) Corrugation profile corresponding to the longer black line in (A).

local solid-solid transformation of the 2H-TaSe₂ crystal induced by the STM tip.

Several important questions are associated with our proposed solid-solid phase transition mechanism: (i) how the H-phase TaSe₂ structure converts to the T-phase, and (ii) how the STM tip interacts with the sample surface to drive this transformation. Correlated motion of Se atoms at the solid-vacuum interface in the topmost layer of H-TaSe₂ could be driven by the electric field of the STM tip. Although the direction of the force arising from the electric field is radially symmetric about the tip, there are three energetically favorable directions for Se atom displacements due to the lattice symmetry. These directions (see Fig. 3A) are [1,0,-1,0], [-1,1,0,0], and [0,-1,1,0]. The minimum displacement to convert H- to T-phase involves collective motion of Se atoms by $(\sqrt{3}/3)a$ along one of the three directions. This displacement converts the trigonal prismatic coordination of H-phase TaSe₂ to the octahedral coordination that typifies the T-phase (Fig. 3, A and B). This change in Ta coordination produces a large change in electronic structure that is manifested by the distinct CDW states of the T- and H-phases. In addition, the T-phase TaSe₂ nanocrystal in our model should be a one-layer single crystal with a small percentage of Se vacancies or adatoms (15).

This model predicts that the Se atoms at the interface will form a rectangular rather than hexagonal structure and that the surface Se rows from the T- and H-phase regions will have a $(\sqrt{3}/6)a$ (≈ 1.0 Å) mismatch at the interface (Fig. 3C). This model also requires no shifting of the Ta sublattice. Analysis of the experimental data (Fig. 3C) shows that the Se atoms at the sharp boundary between T- and H-phase regions define a rectangular cell (16) and that the mismatch of atomic rows in both regions (highlighted by solid lines) is 1.1 ± 0.1 Å. The relatively good agreement between the experimental data and our model indicates that this model should provide a useful framework for understanding this solid-solid phase transition.

We believe that this transformation is driven in large part by the large electric field at the apex of the STM tip. The size of the T-phase nanocrystals increases with increases in the bias voltage used to induce the transformation (Fig. 4, A to C) (17). No transformation from H- to T-phase was observed when the STM tip was brought into contact with the surface or pushed into the surface with low applied voltages. Hence, purely mechanical deformations of the sample cannot drive this structural transformation. In addition, we

do not expect that the estimated temperature rise (18) during the transformation process, 2 to 10 K, will have a significant effect on the mechanism. Moreover, although the intense electric field in STM experiments is localized (~ 10 nm) under the tip position (19), the T-phase nanocrystals created in our studies can be considerably larger in size: 7 to >100 nm. At present, we do not have a detailed explanation for this apparent size mismatch, although it is possible to speculate about

its origin. For example, the structural transformation is likely driven initially in a small region under the tip by electric field-assisted inelastic tunneling (20), but, because relaxation is slow at 4.8 K (that is, there are few phonon modes available), the structural transformation propagates laterally from the region of intense field; the extent of propagation may also be assisted by the weaker field that is present away from the tip apex. The propagation of the structural transformation is

Fig. 3. (A) An atomic model highlighting the initial (purple) and final (green) positions of Se atoms at the surface-vacuum interface in the H- to T-phase transformation. The displacement vectors for each of these Se atoms are denoted by black arrows. These vectors convert the local Ta atom (blue) coordination from trigonal prismatic to octahedral. As illustrated, the Se atoms of this upper sheet are displaced along three directions from the center where the STM tip would be located. The displacements thus create Se atom vacancies that are indicated by filled white circles at the green surface Se atoms. (B) Side views of H (left) and T (right) Se-Ta-Se layers highlighting the trigonal prismatic and octahedral coordination of Ta, respectively. (C) A portion of the model and an experimental image focusing on the interface between T-phase (left) and H-phase (right) TaSe₂ regions. The Se atoms in the surface layer of the H-phase region lie directly on top of the lower sheet of Se atoms. The lines highlight the mismatch of the T-phase and H-phase Se surface lattice rows at the interface. The positions of the Se atoms on the T-phase and H-phase sides of the interface are indicated by small green and purple filled circles, respectively.

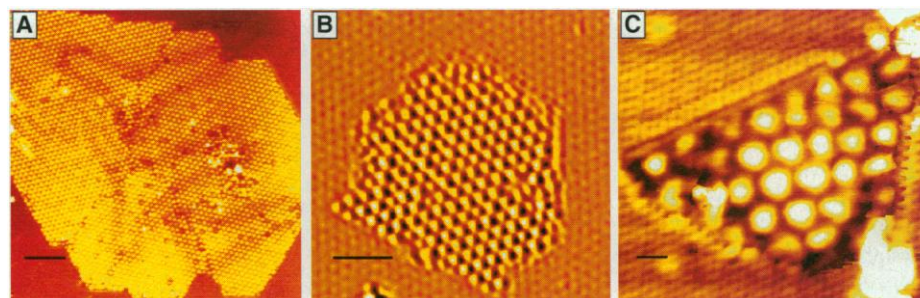
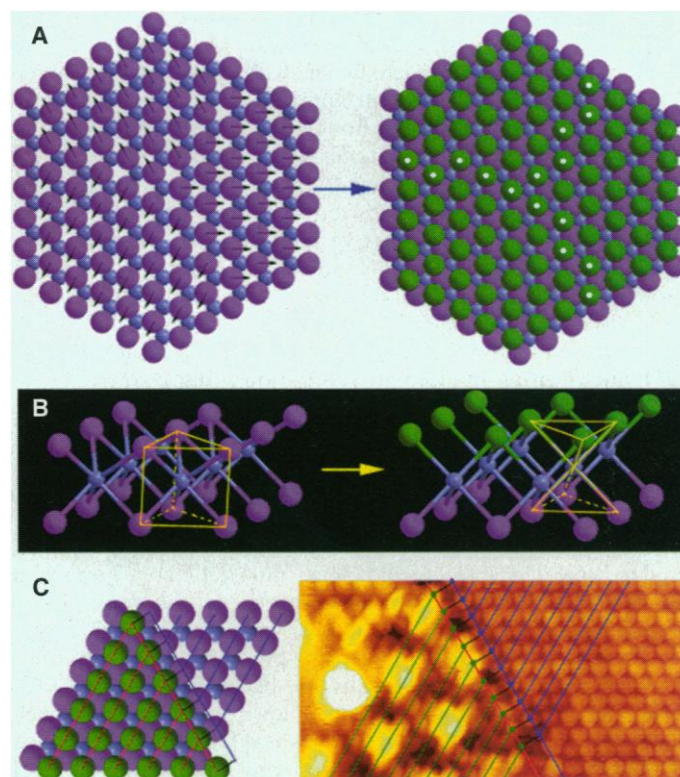


Fig. 4. (A to C) STM images of T-phase TaSe₂ nanocrystals that were created through the use of different applied voltages. The T-phase nanocrystals in these images are all located near the center of the image frame. The nanocrystals were made with modification voltages of -1.40 , -1.30 , and -1.20 mV, respectively. Similar results were also observed with positive applied voltages. Scale bars, 10 nm (A), 5 nm (B), and 1 nm (C).

ultimately limited by the energetic cost of forming Se vacancies (or adatoms), the energy of the growing H-phase–T-phase interface (which is proportional to r , the radius of nanocrystal), and phonon excitations. Further research on the effects of tip-sample separation, voltage pulse duration, and temperature on the creation of nanocrystals should help to elucidate the details of the transformation mechanism.

We believe that the use of the STM to drive solid-solid phase transitions is an exciting approach for the construction of nanocrystals and may also provide interesting opportunities to study solid-solid phase transformations. Fabrication of nanocrystals is usually a challenge with the STM because it is difficult and time-consuming to manipulate the hundreds to thousands of individual atoms needed to construct crystals with nanometer dimensions. In our studies, the fabrication step is simplified through the collective motion of many atoms at once. Earlier work has shown that voltage pulses applied to an STM tip can modify the surface region of materials by field-assisted ion transport (21) and heating-induced crystallization (22); however, these modifications do not correspond to well-defined crystal-crystal transformations and in this regard are distinct from the present work.

Preliminary studies of 2H-TaS₂ and 4H-TaSe₂ showed that the STM can be used to drive a local solid-solid phase transition, which resulted in the formation of T-phase nanocrystals, in these related materials as well. On the basis of the proposed mechanism and our results, we believe the existence of a relatively low-energy pathway (for example, crystal shear of the Se atom layer in TaSe₂) that converts one phase to another is an essential material feature for the STM-driven transformation. More generally, it may be possible to transform layered materials that exhibit distinct crystal phases by using our approach if there is a pathway involving shear of atomic layers between the two phases. We speculate that MoTe₂, which exhibits semiconducting and metallic phases (23), may be transformed in this way.

Our results provide an opportunity for probing the basic physics of CDW formation. It is widely recognized that Fermi surface nesting plays a central role in CDW formation (24). For sufficiently small nanocrystals, the concept of a Fermi surface is, however, not well defined. This has not been an issue in earlier studies of isolated nanocrystals (25) where the essential physics is that of wave function confinement (that is, particle in a box). We have found that it is possible to control the size of T-phase TaSe₂

nanocrystals by varying the applied voltage during the tip-induced modification (Fig. 4). The three T-phase nanocrystals in these images have dimensions of 70, 17, and 7 nm. Qualitatively, the largest T-phase TaSe₂ nanocrystal (Fig. 4A) exhibits a relatively uniform commensurate CDW state. In the smallest T-phase TaSe₂ nanocrystal (Fig. 4C), both the intensity and wavelength of the CDW are obviously distorted relative to the uniform state observed in single crystals or large nanocrystals. The CDW amplitude is larger at the center of the triangular nanocrystal, and the wavelength appears to decrease from ~ 1.2 nm at the center to ~ 1.0 nm at the edge. In our system, T-phase nanocrystals are embedded in the H-phase such that only small distortions in the atomic lattice are expected at the interface between the T- and H-phases. If we assume that the edges of the T-phase nanocrystal are bulk-like, then for symmetric nanocrystals we can apply periodic boundary conditions and recover a pseudo-Fermi surface that mimics the bulk Fermi surface. However, the discreteness of the eigenstates leads to a dispersion in the CDW nesting wave vectors Q not present in the bulk (infinite) system. The dispersion, ΔQ , is $\sim 2\pi/L$, where L is the size of the nanocrystal. In real space, there is a corresponding dispersion in CDW wavelength, $\Delta\lambda \sim \lambda^2/L$. Notably, the wavelength dispersions estimated for the 17 and 7 nm nanoclusters based on our rough Fermi surface model, 0.9 and 2.2 Å, are similar to the dispersion estimated from the experimental images, 1.5 and 2.7 Å, respectively (26).

More experimental and theoretical work is obviously needed if we are to understand fully the effects of size on the collective CDW state. However, we believe that the present results and analysis open an exciting area of nanocrystal research.

REFERENCES AND NOTES

1. D. M. Eigler and E. K. Schweizer, *Nature* **344**, 524 (1990).
2. L. J. Whitman, J. A. Stroscio, R. A. Dragoset, R. J. Celotta, *Science* **251**, 1206 (1991).
3. I.-W. Lyo and Ph. Avouris, *ibid.* **253**, 173 (1991).
4. T. A. Jung, R. R. Schlittler, J. K. Gimzewski, H. Tang, C. Joachim, *ibid.* **271**, 181 (1996).
5. M. F. Crommie, C. P. Lutz, D. M. Eigler, *Nature* **363**, 524 (1993); *Science* **262**, 218 (1993).
6. Ph. Avouris and I.-W. Lyo, *Science* **264**, 942 (1994).
7. J. A. Dagata *et al.*, *Appl. Phys. Lett.* **56**, 2001 (1990); E. A. Dobisz and C. R. K. Marrian, *ibid.* **58**, 2526 (1991).
8. A. D. Kent, T. M. Shaw, S. von Molnár, D. D. Awschalom, *Science* **262**, 1249 (1993); S. Rubel, M. Trochet, E. E. Ehrichs, W. F. Smith, A. L. de Lozanne, *J. Vac. Sci. Technol.* **B12**, 1894 (1994).
9. E. S. Snow and P. M. Campbell, *Science* **270**, 1639 (1995).
10. P. E. Sheehan and C. M. Lieber, *ibid.* **272**, 1158 (1996).
11. J. A. Wilson, F. J. DiSalvo, S. Mahajan, *Adv. Phys.* **24**, 117 (1975).
12. R. V. Coleman *et al.*, *ibid.* **37**, 559 (1988).
13. In the modification procedure, we used several methods. In one, the feedback loop was opened, the tip was advanced a preset amount toward the surface, and then the bias voltage was pulsed or ramped to the desired value. Alternatively, we allowed the z-loop to oscillate (by increasing the gain) for a short time (≤ 100 ms) at the desired voltage value. We were able to create controlled T-phase nanocrystals using both of these methods.
14. The success probability depends on the magnitude of the applied bias voltage and the tip and tunneling junction conditions. At bias voltages exceeding ~ 1.8 V, the success probability for nanocrystal formation is on the order of 90%; this probability drops to zero at the modification threshold voltage, ~ 1.2 V. These values exhibit uncertainty that reflects variations in tip structure and junction conditions.
15. The model in Fig. 3A illustrates the motion of Se atoms in response to a repulsive force that is expected when a negative bias voltage is applied to the STM tip. The Se atom vacancies predicted by our model (with a negative bias) have not yet been observed, although they are expected to be difficult to detect for several reasons. First, the percentage of vacancies is small; we estimated $< 1\%$ vacancies in a single 40-nm T-phase crystal. Second, it is intrinsically difficult to observe all of the atomic sites in T-phase single crystals or nanocrystals because of the strong CDW modulation. In addition, this same model predicts that Se adatoms would be produced when a positive bias voltage was used to drive the transformation (because the Se atom motion would be toward the tip). The small number of adatoms generated in this reverse direction will not be readily observed because they would be expected to exhibit significant mobility on the surface.
16. The experimental data (Fig. 3C) show that the Se atoms at the interface form a rectangular cell that is only slightly distorted from a square, and thus these results contrast with the rectangular model cell suggested by Fig. 3B. The difference between the experimental results and the model is believed to be due to relaxation of the Se atom positions at the interface between the T- and H-phases.
17. These bias voltage-dependent modification experiments were carried out at similar tip-sample separations with electrochemically etched Ir tips. Because the etched Ir tips yield relatively reproducible bias-dependent modifications, which suggest that their shapes are similar, we believe that the major effect of these experiments is a variation in the electric field (which also depends on both the tip-sample separation and the tip shape).
18. B. N. J. Persson and J. E. Demuth, *Solid State Commun.* **57**, 769 (1986).
19. J. A. Stroscio and D. M. Eigler, *Science* **254**, 1319 (1991).
20. B. N. Persson and Ph. Avouris, *Chem. Phys. Lett.* **242**, 483 (1995).
21. A. Sato and Y. Tsukamoto, *Nature* **363**, 431 (1993).
22. U. Stauffer *et al.*, *J. Vac. Sci. Technol.* **A6**, 537 (1988).
23. R. M. A. Lieth and J. C. J. M. Terhell, in *Preparation and Crystal Growth of Materials with Layered Structures*, R. M. A. Lieth, Ed. (Reidel, Boston, 1977), pp. 141–223.
24. R. E. Peierls, *Quantum Theory of Solids* (Oxford Univ. Press, Oxford, 1955), p. 108; H. Fröhlich, *Proc. R. Soc. London Ser. A* **223**, 296 (1954).
25. A. P. Alivisatos, *Science* **271**, 933 (1996).
26. The reported CDW wavelength dispersions correspond to the standard deviation calculated from experimental images. We digitized the images to locate the CDW maxima, and then we used the distances between adjacent maxima to calculate the average and uncertainty in wavelength. The observed experimental uncertainty in roughly infinite crystals was 0.6 Å.
27. We thank E. Kaxiras and F. Spaepen for helpful discussions. The work of C.M.L. was supported under NSF award DMR-9306684.

11 June 1996; accepted 30 August 1996